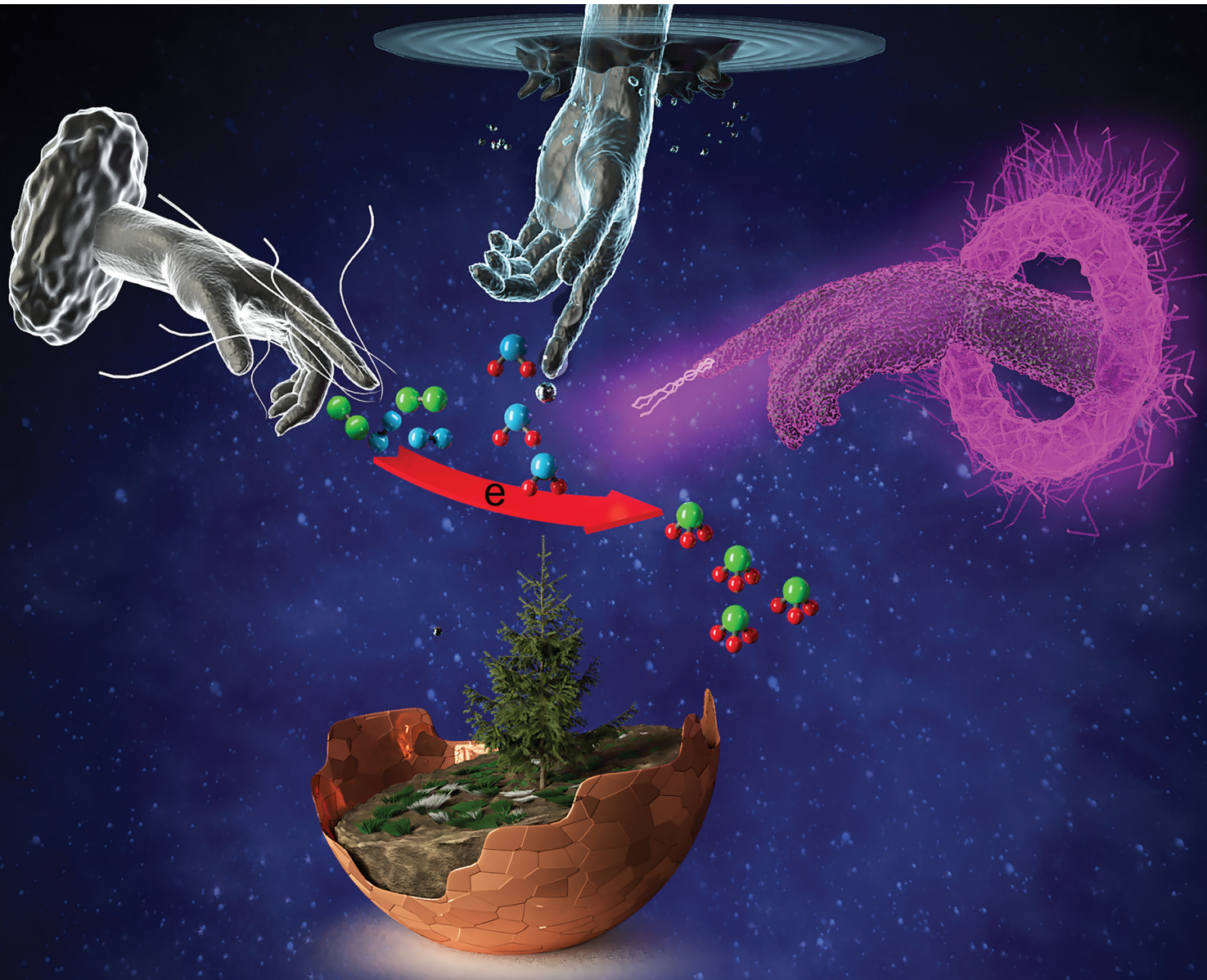


# Energy & Environmental Science

rsc.li/ees



ISSN 1754-5706

## COMMUNICATION

[View Article Online](#)  
[View Journal](#) | [View Issue](#)



Cite this: *Energy Environ. Sci.*, 2021,

14, 865

Received 1st December 2020,  
Accepted 19th January 2021

DOI: 10.1039/d0ee03769a

rsc.li/ees

## A hybrid plasma electrocatalytic process for sustainable ammonia production†

Jing Sun,<sup>a</sup> David Alam,<sup>id</sup> Rahman Daiyan,<sup>id</sup> Hassan Masood,<sup>a</sup> Tianqi Zhang,<sup>id</sup> Renwu Zhou,<sup>id</sup> Patrick J. Cullen,<sup>b</sup> Emma C. Lovell,<sup>id</sup>\*<sup>a</sup> Ali (Rouhollah) Jalili,<sup>id</sup>\*<sup>a</sup> and Rose Amal,<sup>id</sup>\*<sup>a</sup>

From nurturing living organisms to feeding billions of people, the transformation of atmospheric nitrogen to ammonia ( $\text{NH}_3$ ) is essential to sustain life on earth. In nature, bacteria and plants can produce ammonia from air and water at ambient conditions via nitrogen fixation processes. To follow this feat, we couple plasma-driven nitrogen oxides intermediary ( $\text{NO}_x$ ) generation and their electrocatalytic reduction to pave the way for scalable green ammonia at ambient conditions. We developed a non-thermal plasma bubble column reactor that brings together dual reactor configuration with multiple discharge schemes and bubble dynamic control to generate  $\text{NO}_x$  intermediaries at low specific energy consumption of  $3.8 \text{ kW h mol}^{-1}$ . The  $\text{NO}_x$  intermediaries were converted to ammonia at a rate of  $23.2 \text{ mg h}^{-1}$  ( $42.1 \text{ nmol cm}^{-2} \text{ s}^{-1}$ ), using a scalable electrolyzer operating at a low cell voltage of  $1.4 \text{ V}$ , current densities of over  $50 \text{ mA cm}^{-2}$ , and specific energy consumption of  $0.51 \text{ kW h mol}^{-1} \text{ NH}_3$ .

## Introduction

Ammonia ( $\text{NH}_3$ ) production *via* the Haber–Bosch process was one of the critical achievements of the 20th century.  $\text{NH}_3$  production enabled the quadrupling of the output of agricultural products, and recently its potential as an energy vector is increasingly explored.<sup>1</sup> The current Haber–Bosch process is a mature technology which has been utilized and improved on for over a century. Because of this, Haber–Bosch is close to the theoretical energy efficiency of the process.<sup>2</sup> Despite this, the process requires high temperatures ( $>400^\circ\text{C}$ ) and pressures ( $>200 \text{ atm}$ ), as well as pure  $\text{N}_2$  and  $\text{H}_2$  (Fig. 1A). Thus the Haber–

## Broader context

Ammonia ( $\text{NH}_3$ ) is the second most-produced chemical globally used mainly in the fertilizer industry and is directly accountable for feeding around 50% of the world's population. Ammonia has also been recognised as a potential renewable energy carrier and as an excellent hydrogen-storage material. It is more energy efficient to produce, store, and deliver hydrogen as ammonia than as compressed or cryogenic hydrogen. However, the current large scale ammonia production (Haber–Bosch) requires high-temperature and high-pressure and is very energy-intensive. To achieve a green and sustainable ammonia production, we develop a hybrid system that couples the plasma-activation of air to produce nitrates and nitrites ( $\text{NO}_x$ ) intermediates in the water at a high rate and high energy efficiency. The  $\text{NO}_x$  subsequently reduces electrocatalytically to produce ammonia in water (ammonium,  $\text{NH}_4^+$ ) with high selectivity and high faradaic efficiency. The ammonium salt (sulfate or nitrate) can be directly utilized as fertilizer or subsequently converted to ammonia gas. In doing this, we can overcome the limitations of electrocatalytic nitrogen reduction, including the low solubility and stability of atmospheric nitrogen and operate under conditions that can suppress the competing hydrogen evolution reaction. This hybrid plasma/electrocatalytic system is inherently compatible with small scale, de-centralised and on-demand ammonia synthesis.

Bosch process is costly and requires significant plant infrastructure.<sup>3</sup> Because of this, global ammonia production has been established at exclusively a large scale, centralized approach which also requires extensive infrastructure for  $\text{H}_2$  feedstock generation, ammonia transportation and storage. Therefore, there is an immediate need to develop a green alternative process for ammonia production which can be exploited in a small-scale, decentralized, on-demand manner, powered by renewable energy (such as solar and wind).

Recently, the production of  $\text{NH}_3$  through the electrocatalytic nitrogen reduction reaction (eNRR) has gained increasing attention.<sup>4</sup> The eNRR has significant benefits over the Haber–Bosch process, including operating at mild conditions (ambient temperature and pressures), being fundamentally compatible with renewable energy, adaptable to a vast range of scales (from  $\text{kW}$  to  $\text{GW}$ ), well-suited to delocalized production and distribution as

<sup>a</sup> School of Chemical Engineering, University of New South Wales (UNSW), Sydney, Australia. E-mail: e.lovell@unsw.edu.au, ali.jalili@unsw.edu.au, r.amal@unsw.edu.au

<sup>b</sup> School of Chemical and Biomolecular Engineering, University of Sydney, Sydney, Australia

† Electronic supplementary information (ESI) available: Materials and methods, Fig. S1–S22, Tables S1–S4, Movies S1–S6 and Ref. S1–S37. See DOI: 10.1039/d0ee03769a

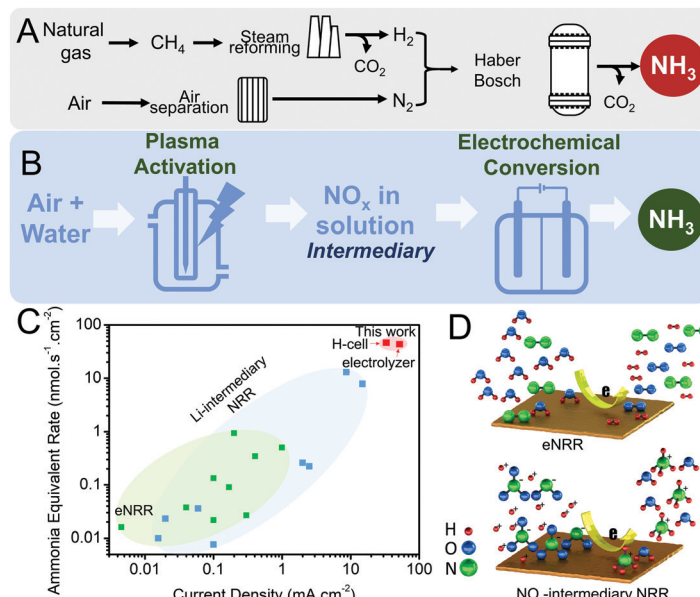


**Fig. 1** Hybrid plasma-electrochemical technology for green ammonia production. Schematics illustrating (A) the Haber–Bosch process and (B) a novel ammonia synthesis approach via  $\text{NO}_x$  intermediaries. Here we use non-thermal plasma to activate water and air, producing  $\text{NO}_x$  dissolved in solution as an intermediary for ammonium's electrochemical synthesis. (C) Reported ammonia equivalent production rate and current densities for our hybrid systems and other NRR systems in the literature. Green squares represent conventional eNRR,<sup>15–23</sup> and blue squares represent Li-intermediary NRR.<sup>7,8,24–28</sup> Detailed data are available in Table S4 (ESI†). Data for the hybrid system developed in this work (using a small H-cell system and a scalable electrolyzer) are shown for comparison (red squares). (D) Schematic illustrating NRR products from  $\text{N}_2$  versus  $\text{NO}_x$  intermediary. The  $\text{NO}_x$  intermediaries are readily converted to ammonium, while the reduction of  $\text{N}_2$ , due to its triple bonds, cannot compete with the HER effectively.

well as not requiring a hydrogen feed.<sup>5</sup> Despite these benefits, the implementation of direct eNRR is intrinsically limited due to the highly unreactive nature of  $\text{N}_2$  and its low solubility in water. Moreover, the eNRR is hampered by competition with the hydrogen evolution reaction (HER), as hydrogen generation usually occurs at a lower overpotential than the eNRR.<sup>6</sup> Consequently, the eNRR remains significantly hindered by low ammonia production rates (typically  $10^{-9}$  to  $10^{-11} \text{ mol cm}^{-2} \text{ s}^{-1}$ ), making reliable detection troublesome and, with few exceptions, very low faradaic efficiencies, below 1%.<sup>7</sup>

A promising approach to overcoming the limitations of eNRR is converting  $\text{N}_2$  into a more reactive intermediary form. In this context, lithium redox intermediary NRR has demonstrated higher rates and current densities than the direct eNRR.<sup>7–9</sup> However, the significant overpotential of a minimum of 3 V for the Li-NRR makes this process inherently energy-intensive. Low system stability, the requirement for expensive ultra-dry and oxygen-free organic solvents, high pressures ( $\sim 50$  bar), pure nitrogen and hydrogen feedstocks, and lithium metal requirements are significant drawbacks of this pathway.

Nitrite and nitrates ( $\text{NO}_3^-$  and  $\text{NO}_2^-$ , respectively) are highly soluble, much more easily reduced to ammonia than  $\text{N}_2$  (Fig. 1D),<sup>10</sup> and benefit from already known chemistry.<sup>11</sup> As such, the generation and exploitation of  $\text{NO}_x$  (a mixture of  $\text{NO}_2^-$  and  $\text{NO}_3^-$  species) as an intermediary to overcome the limitations of  $\text{N}_2$  conversion presents a facile solution to these limitations. However, in industry, nitrites and nitrates are produced from ammonia *via* the Ostwald process. Thus, alternative production pathways need to be developed for generating the  $\text{NO}_x$  intermediary.

Producing nitrogen-containing compounds from air (so-called nitrogen fixation) using thermal plasma was one of the pioneering developed industrial methods. However, the use of plasma for nitrogen fixation was hampered due to the high energy requirement of the thermal plasma-based plants. Plasma processes can be divided into two broad areas, thermal plasma and non-thermal plasma. The technology and energy efficiency of these processes are vastly different. The Birkeland–Eyde process was one of the first approaches of industrial-scale nitrogen fixation for the synthesis of nitric acid. In this process, a thermal plasma arc discharge was used to activate air (with temperatures  $> 3000^\circ\text{C}$ ), followed by quenching with water and a series of adsorption stages. This process yielded nitric acid with an energy consumption of  $\approx 1.15 \text{ kW h mol}^{-1} \text{ HNO}_3$ .<sup>2</sup> Nevertheless, more recent examples of thermal plasma nitrogen fixation, at laboratory scale, have demonstrated significantly higher energy consumptions ranging from 35 to 350  $\text{kW h mol}^{-1}$  of product.<sup>2</sup>

On the other hand, non-thermal plasma is an ionized gas composed of a range of species (including electrons, ions, radicals, molecular fragments) at various energy levels. Non-thermal plasma has been used in several applications ranging from rapid synthesis to surface modification of electrode materials.<sup>12–14</sup> In non-thermal plasmas, high energy electrons with temperatures several orders of magnitudes higher than the surrounding gas are generated. Therefore, it is possible to create high-energy species that can activate atmospheric dinitrogen molecules while keeping the reaction temperature and energy consumption lower compared to the thermal plasmas in

small-scale reactors. To this end, the theoretical energy limit for  $\text{NO}_x$  generation *via* non-thermal plasma is  $5.56 \times 10^{-2} \text{ kW h mol}^{-1} \text{ NO}_x$  (in vacuum). This consumption is at least 2.5 times lower than Haber–Bosch process (0.13 to 0.4  $\text{kW h mol}^{-1} \text{ NH}_3$ ).

Herein, we develop a continuous and scalable plasma-electrochemical hybrid technology for sustainable and facile production of ammonia *via* a  $\text{NO}_x$  intermediary approach (Fig. 1B). Our hybrid technology is based on the coupling between two fundamental aspects: (I) non-thermal plasma-assisted activation of air with much improved rate and energy-efficiency. By understanding the fundamentals of plasma activation, we develop a scalable system that can produce  $\text{NO}_x$  in solution while reducing the specific energy consumption dramatically. (II) The electrochemical conversion of the resultant  $\text{NO}_x$  into ammonium ( $\text{NH}_4^+$ , the water-soluble form of ammonia) at very low cell potentials whilst obtaining considerable  $\text{NH}_4^+$  yields and rate (Fig. 1C).

## Results and discussion

To understand and to optimize the integrated system parameters, the electrocatalytic reduction of  $\text{NO}_x$  to ammonium, the experiments were initially carried out using an integrated system that couple a custom-design plasma-bubbler with an electrochemical H-cell (Fig. 2A and B, refer to ESI† for more detail). It should be noted that herein, plasma-activated electrolyte refers to plasma activation of water containing  $\text{H}_2\text{SO}_4$

(10 mM) using an air bubbler. Preliminary studies were also performed by adding  $\text{NO}_x$  directly into the electrochemical cell to understand the reaction pathways and the role of acid (for more information refer to Fig. S10–S13, ESI†). In acidic media, the reaction proceeds as outlined in ESI† (eqn (S5)–(S8)). Moreover,  $\text{NH}_3$  is soluble in water and can exist as ammonium sulfate and/or ammonium nitrate, which can be directly utilized as fertilizer or be converted to ammonia.

A range of Cu-based catalysts was prepared and evaluated for their performance for the electrocatalytic conversion of  $\text{NO}_x$  to ammonium (Cu foil, foam, and nanowires grown on foam, NWs, for more information refer to Fig. S14, ESI†). We choose Cu due to its stability in the pH and potentials applied herein and its ability to suppress competing HER. Representative scanning electron microscopy (SEM) images of the Cu NWs (Fig. 2C and D) supports the existence of uniformly dispersed thin nanowires (diameters  $\sim 70 \pm 19 \text{ nm}$ ) on the copper foam. It is clear from these images that the Cu NWs seed out from the metallic Cu skeleton of the foam during electrode preparation. When tested, we reveal that the Cu NWs was able to attain the highest current density ( $j$ ) for the reduction of plasma-activated electrolyte whilst achieving an ammonium production rate of  $45 \text{ nmol s}^{-1} \text{ cm}^{-2}$  and faradaic efficiency (FE) of  $\sim 100\%$  (Fig. S14B, ESI†). Comparatively, the Cu foil and foam facilitated much lower FEs of  $\sim 80$  and  $71\%$ , respectively, with ammonium yields of  $6.0$  and  $8.9 \text{ nmol s}^{-1} \text{ cm}^{-2}$  (at  $-0.5 \text{ V}$ ). This inherent improvement in the catalytic activity of Cu NW electrode (compared to Cu foam and foil) can be ascribed to a combination of

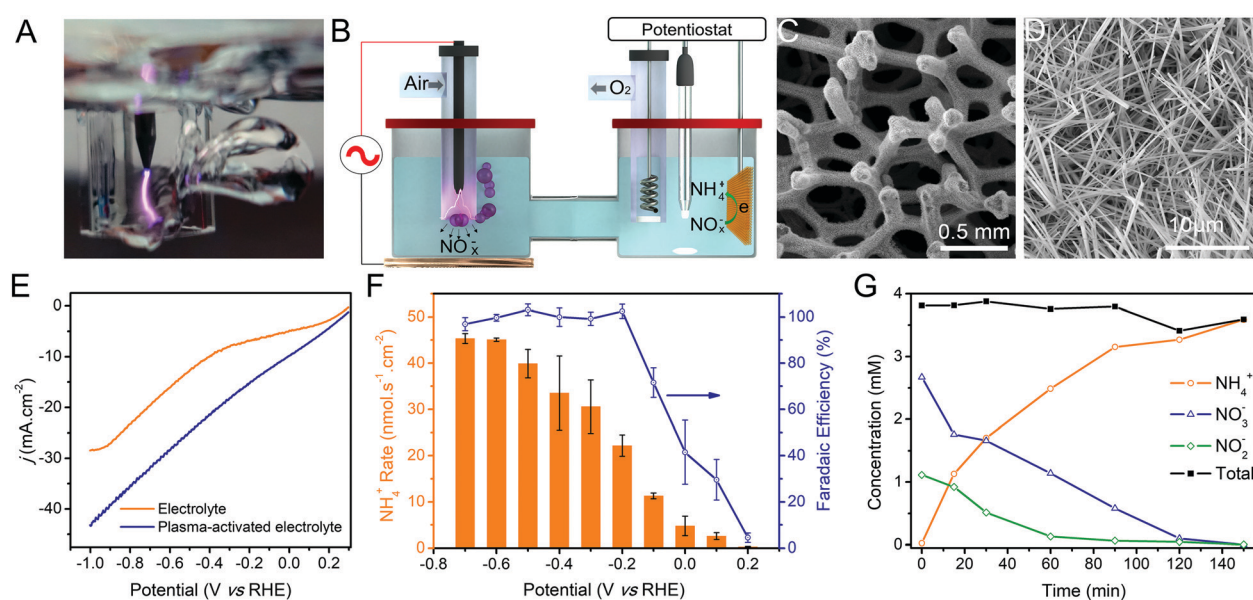


**Fig. 2** A small-scale integrated plasma electrochemical system. (A) Digital photo showing plasma discharge in solution. (B) A schematic showing the small-scale plasma integrated within an H-cell electrochemical system: plasma activation of air, producing  $\text{NO}_x$  dissolved in water (containing 10 mM  $\text{H}_2\text{SO}_4$ ) as an intermediary for the electrochemical synthesis of ammonium in the H-cell. (C and D) Scanning electron microscopy (SEM) pictures of the Cu-NW catalyst. (E) Linear sweep voltammetry (scan rate of  $5 \text{ mV s}^{-1}$ ) comparing the current densities of plasma-activated electrolyte and non-plasma activated electrolyte. (F) Ammonium production rate and faradaic efficiency as a function of applied potential. Please note, no hydrogen was detected via GC connected to the cell. (G) The time-dependent concentration of  $\text{NO}_3^-$ ,  $\text{NO}_2^-$ , and  $\text{NH}_4^+$  during 2.5 h electrolysis of plasma-activated electrolyte at  $-0.5 \text{ V}$  vs. RHE. Note: all the tests were conducted in a custom-designed H-cell using a  $1 \text{ cm} \times 1 \text{ cm}$  Cu-NW electrode and plasma-activated electrolyte without iR correction.

(i) formation of Cu<sup>0</sup>/Cu<sup>+</sup> active sites that suppress HER, (ii) suitable mass-transfer and residence time near nanowire active sites, and (iii) increased amount of active sites, as evidenced from the electrochemical active surface area (ECSA) measurements. XPS measurements (for more information refer to Fig. S1 and S2, ESI†) with Cu NWs reveal the formation of Cu<sup>+</sup>/Cu<sup>0</sup> moieties that may be present on the surface of the nanowire morphology. These interfacial sites are reported to favor nitrate reduction to NH<sub>3</sub>, by reducing the free energy change for the formation of \*NOH radicals.<sup>11</sup> In addition, we find that the ECSA for the Cu NWs catalyst was 120 and 5 times larger than the foil and foam samples, respectively (Fig. S15, ESI†), indicating an increase in active sites for the NWs sample. As such, the formation of these sites in Cu NWs compared to Cu foam and foil can explain the improved ammonium selectivity of the electrode.

To understand the origin of the ammonia, in particular, whether it arises from NO<sub>x</sub>, N<sub>2</sub> reduction, or contaminations, control experiments were performed, showing that the electrolyte (without plasma activation) resulted in no ammonium detection (Fig. S9 and Table S1, ESI†). Further, isotopic tracing (<sup>15</sup>N) indicated that ammonia clearly arose from the NO<sub>x</sub> produced by plasma-activation of <sup>15</sup>N (Fig. S22, ESI†). The polarization curves (Fig. 2E) revealed that the electrocatalytic NO<sub>x</sub> reduction facilitated a very high current density (*j*), attaining a *j* of  $-45\text{ mA cm}^{-2}$  at  $-1\text{ V}$  (compared to  $28\text{ mA cm}^{-2}$  for the non-plasma activated electrolyte). This indicates that the higher current obtained arises from NO<sub>x</sub> reduction.

Fig. 2F displays the dependence of ammonium production rate and FE for NO<sub>x</sub> reduction on applied potential (each electrolysis duration was 0.25 h). As the potential was changed from 0.2 V to  $-0.6\text{ V}$ , the ammonia production (measured as NH<sub>4</sub><sup>+</sup>) rate increased along with the FE (from 5% at 0.2 V to  $\sim 100\%$  at  $-0.2\text{ V}$ ). The lower FE (<100%) between 0.2 V to  $-0.2\text{ V}$  can be ascribed to the charge used for the conversion of NO<sub>3</sub><sup>-</sup> to NO<sub>2</sub><sup>-</sup> species. During NO<sub>3</sub><sup>-</sup> reduction, generation of \*NO<sub>2</sub> is a key intermediary.<sup>11</sup> We observed a portion of the \*NO<sub>2</sub> desorbed into the solution as NO<sub>2</sub><sup>-</sup> at lower potentials (for more information refer to Fig. S12 and S13, ESI†), hence the observed lower FE at lower potentials (between 0.2 to  $-0.2\text{ V}$ ). At higher potentials, however, the conversion rate of both nitrate and nitrite to ammonia is high; therefore, the produced nitrite is subsequently converted to ammonia.<sup>11</sup> Note that our applied potentials are higher than water splitting potential and the theoretical potential for NO<sub>3</sub><sup>-</sup> and NO<sub>2</sub><sup>-</sup> owing to sluggish reaction kinetics at low overpotential which restrict yield.

To further understand the reaction pathway, and the consumption of both nitrate and nitrite as a function of electrolysis duration, a batch experiment was undertaken with a successive sampling of nitrite, nitrate, and ammonia (Fig. 2G). With an extended reaction time of 2.5 h, both NO<sub>3</sub><sup>-</sup> and NO<sub>2</sub><sup>-</sup> species were exhausted entirely (from 2.7 and 1 mM, respectively). Simultaneously the ammonia concentration increased from 0 to 3.5 mM. The total concentration of N-species remained constant during electrolysis whilst the FE remained at  $\sim 100\%$  for the first 1 h then slowly declined. This was attributed to the

consumption of reactive NO<sub>x</sub> being converted entirely into ammonia (consistent with the decline in *j* shown in the chronoamperometric *i-t* curve (Fig. S16, ESI†)). Importantly, post-reaction assessment of the Cu NWs cathode through X-ray photoelectron spectroscopy (XPS) revealed no noticeable chemical changes in the electrode (Fig. S1 and S2, ESI†). Moreover, the N1s spectrum did not indicate any nitrogen bound to the surface of the cathode, indicating the non-poisoning interaction of the NO<sub>x</sub> reactive species with the catalyst (Fig. S3, ESI†).

With the H-cell proof-of-concept system clearly indicating the capability of plasma-driven NO<sub>x</sub> generation and subsequent electrocatalytic reduction to ammonia, a scalable plasma bubble column reactor was developed with the focus on its energy efficiency with respect to NO<sub>x</sub> formation. The use of underwater plasma bubbles is attractive for intensification of gas-to-liquid mass transfer, which is assisted by interfacial areas, residence time, and internal pressures.<sup>29</sup> Thus, we developed a non-thermal AC plasma, exploiting a bubble column with varying discharge regimes (including spark and glow discharges). By exploiting these parameters, the scaled plasma bubble column reactor achieved a large increase in NO<sub>x</sub> energy efficiency, attaining a NO<sub>x</sub> generation at a specific energy consumption of  $64\text{ kW h kg}^{-1}$  ( $3.8\text{ kW h mol}^{-1}$ ), which is at least three times better than the best report<sup>30</sup> (Table S4d, ESI†). The theoretical energy limit for dinitrogen oxidation is reported to be  $5.56 \times 10^{-2}\text{ kW h mol}^{-1}$  for pressures in ranges 10 to 100 torr, albeit mathematical evaluation for atmosphere pressure plasmas (used in our work) has not been performed. In the case of scalability, plasma-bubble technology is known to exhibit considerable potential to scale NO<sub>x</sub> production, which is also substantiated by the linear increase in NO<sub>x</sub> generation with time in Fig. S21 (ESI†).

In order to understand the features of the scaled plasma bubble column reactor, and how they resulted in improved energy efficiencies obtained, five different design configurations (Fig. 3A–C and Fig. S17 and Videos S1–S5, ESI†) were developed and evaluated, with underwater plasma bubbles as the dominating aspect of the designs. The generation of plasma, within bubbles (Fig. 3C and Video S6, ESI†), allows for a reduction in breakdown voltage yielding chemical species at lower energy inputs. Also, it facilitates practical interfacing and scaling of plasma discharges with liquids. Optical emission spectra (OES, Fig. S18, ESI†) provide key insights into the differing excitation pathways between the glow and spark discharges. The excited species generated in the glow discharge differ drastically from those in the spark discharge (Fig. 3D). Within a glow discharge system, NO<sub>3</sub><sup>-</sup> is the dominant species (SRGD) produced, whilst with the spark discharge, NO<sub>2</sub><sup>-</sup> is favored (SRSD). This change in excited species for the spark discharge can be attributed to the presence of an air/water interface. Combining the two forms of discharges within a single unit made efficient utilization of the applied power minimizing energy losses (Table S1, ESI†). The power input is not increased significantly with both discharge regimes; however, the generation of species is greatly enhanced as the glow

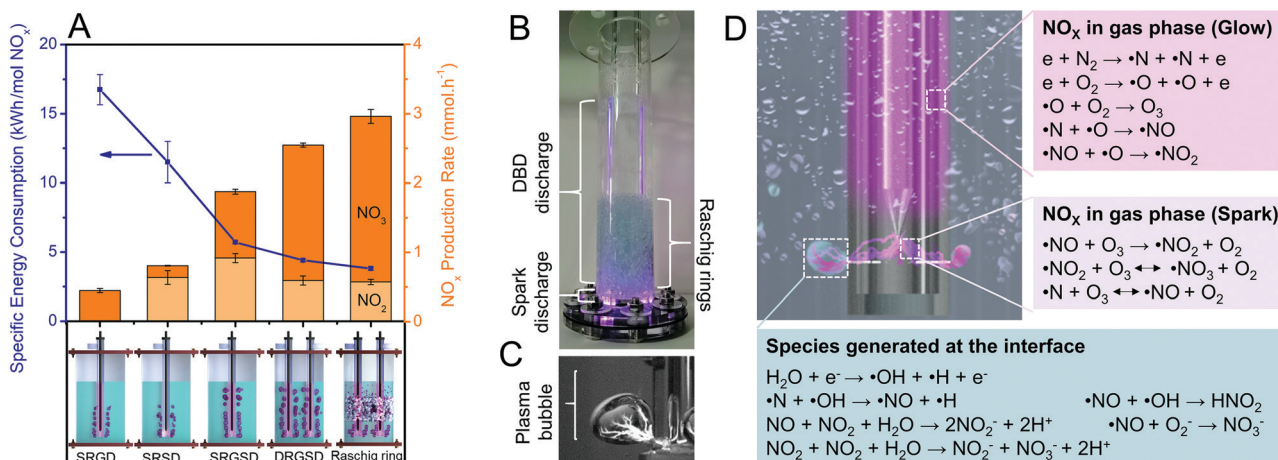


**Fig. 3** Plasma reactor design and busting system performance. (A) Specific energy consumption and NO<sub>x</sub> production rate with schematics representing plasma bubble column reactors design configurations: single reactor glow discharge (SRGD); single reactor spark discharge (SRSD); single reactor glow and spark discharge; double reactor glow and spark discharge (DRGSD); and DRGSD with Raschig rings. (B) Photo showing the combined double reactor glow and spark discharge with Raschig rings and (C) a plasma bubble representative photo. (D) Schematic outlining proposed pathway and excited species in the DRGSD reactor with Raschig rings with species detected through OES (Fig. S18, ESI†).

discharge acts as an excitation pre-treatment prior to the spark discharge. Further, the implementation of dual reactors (one connected to the positive terminal, the other to the negative terminal) resulted in improved NO<sub>x</sub> species generation and energy efficiency. This is because in the single reactor configurations, the positioning of the negative electrode on the outside of the reactor wall leads to energy losses at this electrode, including the generation of micro-discharges which are not utilized in the reaction. Besides, the ratio of NO<sub>2</sub><sup>-</sup>/NO<sub>3</sub><sup>-</sup> shifts because of variability in energetic discharge in the second reactor compared to the first reactor. The incorporation of Raschig rings further increased energy efficiency. This enhancement can be attributed to the provision of a large surface area for gas–liquid interaction. The improved mass transfer and residence times allowed for an intensification of transport of gas-phase NO<sub>x</sub> species into solution. Thus, the key features of our reactor design, leading to high energy efficiencies, are characterized by the combination of (a) multiple discharge schemes (glow and spark discharges) (b) dual reactor configuration within one AC circuit; and (c) bubble dynamics control (Raschig rings). Ultimately, these key design approaches resulted in an energy-efficient and scalable approach to aqueous NO<sub>x</sub> production.

The two different plasma discharge regimes induced in the reactor lead to a broad range of mechanistic pathways for NO<sub>x</sub> production from air, as highlighted in Fig. 3D. Glow discharges in the tubular reactor region primarily contribute to activating N<sub>2</sub> and O<sub>2</sub> molecules to form excited N, N<sub>2</sub> (vibrational states), O, O<sub>2</sub> and O<sub>3</sub> species, as well as a small amount of NO<sub>x</sub>, whilst spark discharges in the forming bubbles cause higher energy levels providing a highly reactive environment for NO<sub>x</sub> formation, as evidenced from the OES data (Fig. S18, ESI†). The 9.8 eV strong triple bond of N<sub>2</sub> can be broken by vibrational excitation, followed by the reaction with O atoms or O<sub>2</sub> molecules to form NO<sub>x</sub>. In the spark discharge regime, O<sub>3</sub> is mainly quenched by NO, of which the production rate is proportional to the N<sub>2</sub>

vibrational temperature. The interactions between plasma and liquids are favorable for the generation of OH radicals and further delivery of the generated reactive species (NO<sub>x</sub>) into solutions.<sup>31</sup>

The NO<sub>x</sub> solution (1.2 mM of NO<sub>x</sub>) generated from the high rate and superior energy-efficient plasma reactor was then fed to a custom-designed electrolyzer with our developed Cu-NW catalyst (9 cm<sup>-2</sup>) (Fig. 4A). This allows a high production rate of green ammonia as well as an understanding of the impact of potential and current density to determine the most economical conditions for future manufacturing. Our results reveal that ammonium can be produced at up to 24 mg h<sup>-1</sup> (Fig. 4B) at a current density of 52 mA cm<sup>-2</sup> and cell voltage as low as 1.4 V.

We showcase an integrated system that is not constrained by the non-reactivity and low solubility of nitrogen gas. The integrated system paves the way to the realization of renewable electrocatalytic systems for ammonia production at scalable operating currents, rate and energy consumption needed for industrial applications. The long-term stability of ammonia production is an essential factor that relies on the stable generation of the NO<sub>x</sub> intermediary followed by their conversion to ammonium via the electrolyzer. Fig. S21 (ESI†) shows plasma generated NO<sub>3</sub><sup>-</sup> and NO<sub>2</sub><sup>-</sup> in the column bubbler as a function of time. The total concentration of NO<sub>x</sub> increases linearly as a function of plasma activation time. This gives us the flexibility to match the required feed for the electrolyzer. Subsequently, we studied the stability of the flow system at a current density of 30 mA cm<sup>-2</sup>, where plasma-activated electrolyte was fed continuously while ammonia as NH<sub>4</sub><sup>+</sup> was collected from the outlet. The hybrid system maintained a stable applied cell voltage of 1.50 ± 0.04 V whilst the production rate started from ~20 mg h<sup>-1</sup> (first 0.25 h) then stabilized at ~12.5 mg h<sup>-1</sup> after the first 2 h (Fig. 4C). The reduction in the ammonium rate can be attributed to charge loss due to the conversion of nitrate to nitrite as well as potential physical damage to the Cu

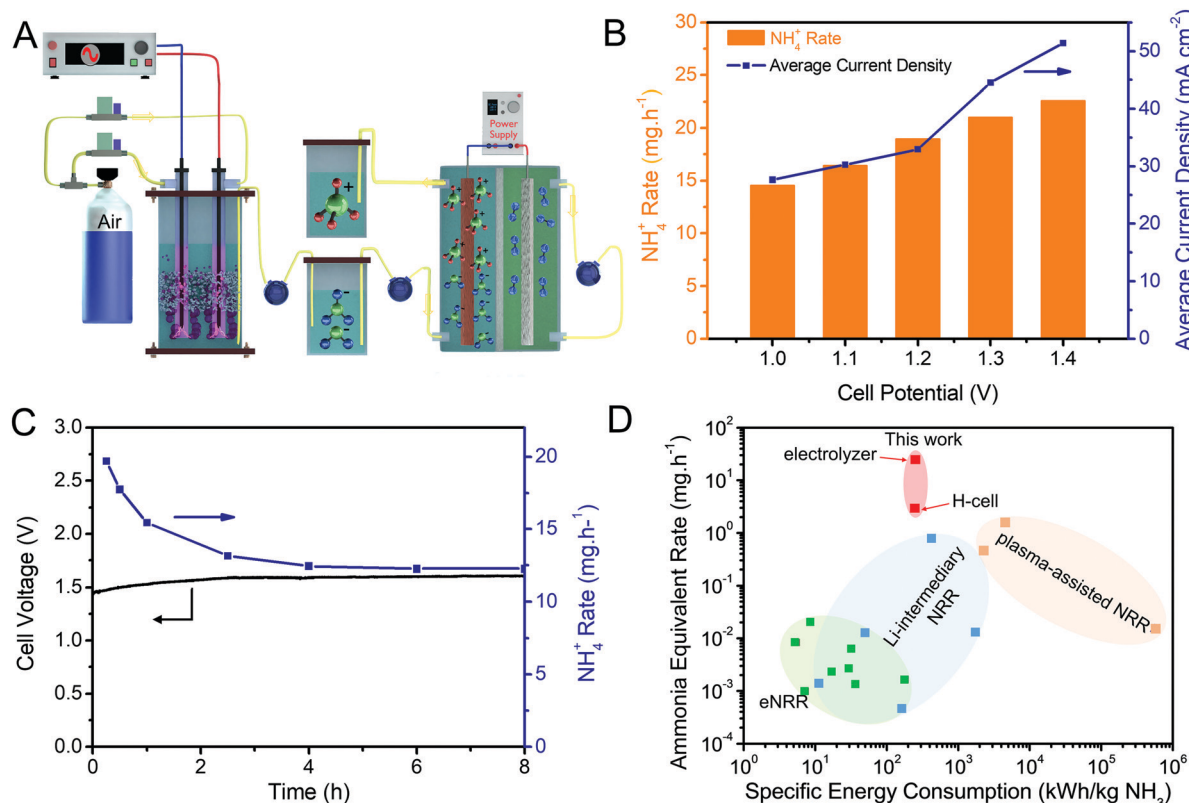


Fig. 4 The hybrid flow-through plasma-electrolyzer system with high energy efficiency and ammonia production rate. (A) A schematic of the flow-through system with the plasma bubble column reactor having a liquid outlet leading to the electrolyzer to convert the  $\text{NO}_x$  to  $\text{NH}_4^+$ . (B)  $\text{NH}_4^+$  production rate and current density as a function of cell voltage. (C) Cell potential and  $\text{NH}_4^+$  production rate over 8 hours at  $30 \text{ mA cm}^{-2}$ . (D) Ammonia equivalent production rate and energy consumption for our system and other NRR systems in the literature, green squares represent direct eNRR,<sup>15–23</sup> and blue squares represent Li-intermediary,<sup>7,8,24–28</sup> and brown squares for plasma-assisted NRR.<sup>32,33</sup> Data for the hybrid system demonstrated in this work are shown for comparison (red squares). Detailed data can be found in Table S4 (ESI†).

NWs under constant flow at the beginning of the experiment. However, afterward, the production rate stabilized across the 6 h.

Fig. 4D compares the overall production rate of ammonia with recently reported state-of-art results for eNRR, Li-intermediary NRR, and plasma-assisted NRR demonstrated at ambient conditions. The  $\text{NO}_x$  intermediary approach developed in this study yields the highest rates of ammonia production while maintaining low specific energy consumption. The ammonia yield rate is between one to three orders of magnitude higher than every other electrochemical method (at similar reaction geometric areas). When scaled up using an electrolyzer, the rate is further increased by another order of magnitude. At the same time, this hybrid system is characterized by a specific energy consumption that is lower than other competing emerging technologies ( $3.8 \text{ kW h mol}^{-1}$  for conversion of air to  $\text{NO}_x$  plus  $0.51 \text{ kW h mol}^{-1}$   $\text{NO}_x$  to  $\text{NH}_4^+$ ; a total of  $4.31 \text{ kW h mol}^{-1}$   $\text{NH}_3$ , equivalent to  $253 \text{ kW h kg}^{-1}$   $\text{NH}_3$ ). This is between one to three orders of magnitude less energy-intensive than plasma-assisted electrochemical conversion of nitrogen to ammonia and gas-phase Dielectric Barrier Discharge (DBD) synthesis method (Table S4a and c, ESI†). In addition to the lower energy consumption and high durability,

the ammonia production rate is  $\sim 30$  times more than the highest reported ammonia production rate *via* Li-intermediary approaches (Table S3b, ESI†). In the case of direct eNRR, no approach has been demonstrated to show a meaningful production rate and FE, making those systems not feasible for any practical application.

## Conclusions

We tackle the grand challenge of green ammonia production by exploring a facile approach that overcomes the low solubility and intrinsic unreactivity of atmospheric dinitrogen. Herein, we develop a continuous, scalable, high energy efficient and stable hybrid technology for a high production rate of ammonia-based on the coupling plasma-assisted activation of  $\text{N}_2$ ; and electrocatalytic conversion of relevant plasma species to ammonia. This process requires only air and water as the two key reactants and produces aqueous phase ammonia. The low energy consumption and high production rate, compared to the similar technologies, coupled with the cheap and abundant inorganic materials exploited herein to ensure the process is inherently scalable. This hybrid process

facilitates on-site, decentralized production of ammonia, that can be powered by cheap surplus renewable resources (such as solar or wind). The systematic improvements in energy efficiency herein provides a leap forward reviving large-scale chemical synthesis using plasma. The generation of plasma within bubbles promotes diffusion of  $\text{NO}_x$  in liquid with promising scalability potential. Multiple discharge regimes generated *via* AC pulses at controllable duty cycle improved energy utilization by suppressing unwanted collisions, yielding chemical species at lower energy inputs. Dual plasma reactors within a single AC-circuit further enhanced the energy efficiency of the process by mitigating energy losses at the ground electrode. Moreover, as the non-thermal plasma demonstrates the lowest theoretical limit of power consumption for nitrogen fixation, this route has the most potential as an alternative to HB process. Ultimately, this technology has the potential to pave the way for green ammonia production and can also be applied to a range of more complex electrocatalytic synthesis system where their performances are limited by reactivity, stability and/or solubility of the reactant molecules.

## Author contributions

R. A., E. C. L. and R. J. conceptualized the study and led the project. J. S. performed the bulk of the experiments and characterization with R. J. R. D. contributed to catalyst characterization, electrochemical analysis and electrolyzer testing. P. J. C., D. A., R. Z., T. Z. and H. M. designed, experiment and characterized the plasma reactors. All authors contributed to the writing of the manuscript and data analysis.

## Conflicts of interest

Author Patrick Cullen is the CEO of PlasmaLeap Technologies, the supplier of the plasma power source used in this study.

## Acknowledgements

This work was financially supported by the Australian Research Council under the Discovery Early Career Research Award (DE180100215) and the Laureate Fellowship Scheme (FL140100081). The authors would like to acknowledge the financial support received from the Office of the Deputy Vice-Chancellor, the University of Sydney and gratefully acknowledge the facilities provided by the UNSW Mark Wainwright Analytical Centre.

## Notes and references

- 1 R. M. Nayak-Luke and R. Banares-Alcantara, *Energy Environ. Sci.*, 2020, **1**, 1–10.
- 2 N. Cherkasov, A. O. Ibhadon and P. Fitzpatrick, *Chem. Eng. Proc. Intensif.*, 2015, **90**, 24–33.
- 3 M. S. Vasileios Kyriakou, I. Garagounis, A. Vourros and E. Vasileiou, *Joule*, 2020, **4**, 142–158.
- 4 T. M. Gur, *Energy Environ. Sci.*, 2018, **11**, 2696–2767.
- 5 J. Kibsgaard, J. K. Nørskov and I. Chorkendorff, *ACS Energy Lett.*, 2019, **4**, 2986–2988.
- 6 D. R. Macfarlane, J. Choi, B. H. R. R. Suryanto, R. Jalili, M. Chatti, L. M. Azofra and A. N. Simonov, *Adv. Mater.*, 2020, **1904804**, 1–13.
- 7 S. Z. Andersen, V. Čolić, S. Yang, J. A. Schwalbe, A. C. Nielander, J. M. McEnaney, K. Enemark-Rasmussen, J. G. Baker, A. R. Singh, B. A. Rohr, M. J. Statt, S. J. Blair, S. Mezzavilla, J. Kibsgaard, P. C. K. Vesborg, M. Cargnello, S. F. Bent, T. F. Jaramillo, I. E. L. Stephens, J. K. Nørskov and I. Chorkendorff, *Nature*, 2019, **570**, 504–508.
- 8 N. Lazouski, M. Chung, K. Williams, M. L. Gala and K. Manthiram, *Nat. Catal.*, 2020, **3**, 463–469.
- 9 J. M. McEnaney, A. R. Singh, J. A. Schwalbe, J. Kibsgaard, J. C. Lin, M. Cargnello, T. F. Jaramillo and J. K. Nørskov, *Energy Environ. Sci.*, 2017, **10**, 1621–1630.
- 10 X. Zhang, Y. Wang, C. Liu, Y. Yu, S. Lu and B. Zhang, *Chem. Eng. J.*, 2021, **403**, 126269.
- 11 Y. Wang, W. Zhou, R. Jia, Y. Yu and B. Zhang, *Angew. Chem.*, 2020, **132**, 5388–5392.
- 12 B. Ouyang, Y. Zhang, X. Xia, R. S. Rawat and H. J. Fan, *Mater. Today Nano*, 2018, **3**, 28–47.
- 13 H. Liang, F. Ming and H. N. Alshareef, *Adv. Energy Mater.*, 2018, **1801804**, 1–24.
- 14 Y. Zhang, R. S. Rawat and H. J. Fan, *Small Methods*, 2017, **1700164**, 1–7.
- 15 B. H. R. Suryanto, A. Mesa, R. Douglas, S. Bhr, D. Wang, A. Lm, M. Harb and L. Cavallo, *ACS Energy Lett.*, 2019, **4**, 430–435.
- 16 M. Shi, D. Bao, B. Wulan, Y. Li, Y. Zhang and J. Yan, *Adv. Mater.*, 2017, **29**, 2–7.
- 17 L. Zhang, L. Ding, G. Chen, X. Yang and H. Wang, *Angew. Chem.*, 2019, **510640**, 2638–2642.
- 18 D. Bao, Q. Zhang, F. L. Meng, H. X. Zhong, M. M. Shi, Y. Zhang, J. M. Yan, Q. Jiang and X. B. Zhang, *Adv. Mater.*, 2017, **29**, 1–5.
- 19 H. Jin, L. Li, X. Liu, C. Tang, W. Xu, S. Chen and L. Song, *Adv. Mater.*, 2019, **1902709**, 1–8.
- 20 J. Wang, L. Yu, L. Hu, G. Chen, H. Xin and X. Feng, *Nat. Commun.*, 2018, **9**, 1795.
- 21 S. Chen, S. Perathoner, C. Ampelli, C. Mebrahtu, D. Su and G. Centi, *Angew. Chem.*, 2017, **129**, 2743–2747.
- 22 S. J. Li, D. Bao, M. M. Shi, B. R. Wulan, J. M. Yan and Q. Jiang, *Adv. Mater.*, 2017, **170001**, 1–6.
- 23 S. Mukherjee, D. A. Cullen, S. Karakalos, K. Liu, H. Zhang, S. Zhao, H. Xu, K. L. More, G. Wang and G. Wu, *Nano Energy*, 2018, **48**, 217–226.
- 24 N. Lazouski, Z. J. Schiffer, K. Williams and K. Manthiram, *Joule*, 2019, **3**, 1127–1139.
- 25 H. K. Lee, C. Sher, L. Koh, Y. H. Lee, C. Liu and I. Y. Phang, *Sci. Adv.*, 2018, **3208**, 1–9.
- 26 K. Kim, J. E. Soc, K. Kim, C. Yoo, J. Kim, C. Yoon and J. Han, *J. Electrochem. Soc.*, 2016, **163**, 1523–1526.
- 27 T. M. Pappenfus, K. Lee, L. M. Thoma and C. R. Dukart, *ECS Trans.*, 2009, **16**, 89–93.

- 28 G. Chen, X. Cao, S. Wu, X. Zeng, L. Ding and M. Zhu, *J. Am. Chem. Soc.*, 2017, **139**, 9771–9774.
- 29 B. S. Sommers and J. E. Foster, *Plasma Sources Sci. Technol.*, 2014, **23**, 015020.
- 30 K. Tachibana and T. Nakamura, *J. Phys. D: Appl. Phys.*, 2019, **52**, 385202.
- 31 R. Zhou, R. Zhou, K. Prasad, Z. Fang, R. Speight, K. Bazaka and K. Ostrikov, *Green Chem.*, 2018, **20**, 5276–5284.
- 32 R. Hawtof, S. Ghosh, E. Guarr, C. Xu, R. M. Sankaran and J. N. Renner, *Asian J. Chem.*, 2019, **31**, 1–10.
- 33 S. Kumari, S. Pishgar, M. E. Schwarting, W. F. Paxton and J. M. Spurgeon, *Chem. Commun.*, 2018, **54**, 13347–13350.